Hover Stand Development Enabling Expanded Experimental Capabilities for Mars Rotors

B. Natalia Perez Perez[1,2], Haley V. Cummings[1,3], Witold J. F. Koning[1,4], Farid B. Haddad[5], Alex L. Sheikman[1,6], Charles J. Cornelison[1,7], Alfredo Perez[1,8], Antonio Cervantes[1,9]

[1] *NASA Ames Research Center, Moffett Field, CA 94043*

[2] *Aerospace and Mechanical Engineer, Analytical Mechanics Associates*

[3] *Mechanical Engineer*

[4] *Aerospace Engineer, Analytical Mechanics Associates*

[5] *Controls Engineer, United States Air Force, Moffett Field, CA 94043*

[6] *Instrumentation Engineer*

[7] *Aerospace Engineer*

[8] *Engineering Technician, Jacobs Engineering*

[9] *PAL Facility Manager*

This paper presents the design and validation of the Rotor Optimization for the Advancement of Mars eXploration (ROAMX) Hover Test Stand, a vacuum compatible stand developed to measure rotor performance under Mars aerodynamic conditions. The stand integrates a high-speed water-cooled motor, a variable pitch hub, and a structural safety system capable of withstanding the high loads resulting from rotor blade loss while enabling continued experimental operations. The stand also maintains the measurement fidelity required for thrust and torque characterization at low Reynolds number. Aerodynamic blockage was limited to less than 20% through geometric constraints on the stand architecture. Calibration and sensor procedures ensured correct load transfer through the intended structural load path and also verified sensor accuracy. Test Entry 1 demonstrated successful test stand performance and testing of experimental blades. The stand spun blades to 4,000 Revolutions per Minute (RPM) for Test Entry 1, but the motor is capable of continuous operation at 5,900 RPM. The ROAMX Hover Test Stand provides a reusable experimental capability that enables high-fidelity evaluation of Mars rotor designs.

I. Introduction

With the success of the Ingenuity Mars Helicopter (Figure 1) demonstrating that powered flight is possible on Mars in 2021 [1], interest in designing more capable helicopters for future exploration of the Red Planet has significantly increased. At NASA Ames Research Center, extensive work has been conducted through the Rotor Optimization for the Advancement of Mars eXploration (ROAMX) project to advance the understanding of Martian aerodynamics and to design airfoils and rotor blades optimized specifically for flight under Mars aerodynamic conditions [2–8].

Complementing these computational design efforts, experimental investigations and high-fidelity Computational Fluid Dynamics (CFD) studies conducted in collaboration with Tohoku University and Imperial College London have validated the increased performance of a set of ROAMX

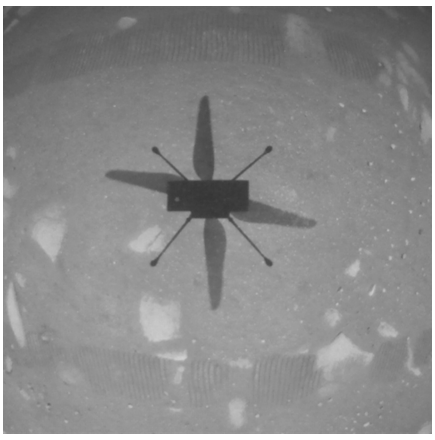

Fig. 1 Ingenuity's shadow from the first-ever powered flight on another planet [1].

Presented at the Vertical Flight Society's Vertical Lift Aircraft Design & Aeromechanics Specialist's Conference, San Jose, CA, USA, Jan. 27-29, 2026.

optimized airfoils relative to the baseline Ingenuity airfoil [9, 10]. This body of research culminated in a full-scale hover test of ROAMX rotor blades under Mars atmospheric density conditions within the Planetary Aeolian Laboratory (PAL) at NASA Ames [11, 12]. The experimental results confirm that the ROAMX rotor achieves higher aerodynamic performance than the Ingenuity baseline rotor when operated in an identical configuration at Mars aerodynamic conditions.

Conducting this experimental campaign required the development of a new test capability: a stand able to spin the rotor at high tip Mach numbers, operate continuously in a vacuum environment, accurately measure rotor thrust and torque at Mars density, and since the stand was designed to test experimental rotors, have the ability to withstand loss of a blade and continue operation with minimal downtime. To satisfy these requirements, a dedicated stand was designed, analyzed, manufactured, and validated specifically for ROAMX testing.

Beyond enabling the ROAMX hover campaign, the resulting test stand now provides a repeatable, easy to operate, and facility-integrated capability for future Mars rotor experiments. Its robust measurement system, vacuum-compatible design, and the ease with which rotor types can be swapped, substantially reduce the setup time, operational risk, and cost typically associated with Mars rotor testing. As such, the stand represents not only a key enabler of ROAMX but a long-term experimental asset for NASA and the broader rotorcraft community, supporting rapid evaluation of emerging Mars rotor concepts for years to come.

This paper describes the development of this test stand, including the design requirements and approach, instrumentation strategy, and facility integration while highlighting the operational capability it establishes for ongoing and future Mars helicopter research.

II. Design Philosophy and Development Approach

To guide the development of the ROAMX Hover Test Stand (RHTS) and ensure it could reliably support Mars density rotor testing, a clear set of test requirements was first established based on aerodynamic, structural, and facility constraints.

The primary objective of the ROAMX experimental campaign was to obtain high-fidelity rotor performance measurements under atmospheric conditions representative of Mars. A secondary objective was to enable a reliable, easy-to-use capability for future Mars rotor experiments within the PAL facility. Achieving these objectives imposed a set of environmental, aerodynamic, structural, and instrumentation requirements on the test stand and associated facility hardware. These requirements ensured that the stand could operate safely and reliably within the PAL vacuum chamber at near-vacuum while producing accurate and repeatable data suitable for validating rotor designs and informing future Mars helicopter concepts. A summary of the capabilities of the ROAMX test stand can be found in Table 1.

A. Design Constraints

The design of the ROAMX test stand was guided by requirements for measurement accuracy, structural reliability, vacuum compatibility, and efficient test operations. Achieving accurate thrust and torque measurements under Mars aerodynamic conditions required a well-defined load path, with instrumentation capable of resolving low aerodynamic forces while withstanding not only nominal loads, but also the high loads in the event of a blade loss.

Vacuum compatibility of test stand components was also a design constraint. All sensors, as well as the motor and actuator assemblies, were specified for vacuum operation, and the bearing lubricants were selected for low-pressure compatibility.

Finally, the stand needed to handle off-nominal conditions safely and predictably. The structural layout, load paths, and sensor mounting locations were chosen to limit damage in the event of rotor imbalance or component failure and to enable quick return to test operations. These principles established the basis for the structural, mechanical, and instrumentation design decisions described in the following sections. Table 2 lists the density and RPM that were tested in Test Entry 1. The test stand is designed to be spun up to 0.95 tip Mach number, which is equivalent to 4300 RPM for a 1.4 m diameter rotor (the diameter of the ROAMX rotor). An overview of the components that make up the mechanical system of the test stand can be seen in Figures 2, 3, and 4.

B. Mars Aerodynamic Conditions

To replicate the aerodynamic environment experienced by a rotor on Mars, the test stand was required to operate at chamber pressures corresponding to a density range of approximately 0.009–0.025 kg/m^3, consistent with a range of Mars surface conditions that would be experienced by a helicopter. Stable pressures were necessary to ensure that the Reynolds number remained stable throughout each test. The resulting pressure in the PAL facility was between $5-30$ mbar, and all components incorporated on the test stand were required to be able to operate at the near-vacuum conditions experienced. Although outgassing is not a primary concern since the PAL is not a clean facility, the reduced-pressure environment affects lubrication behavior and thermal response.

Vacuum operation places specific constraints on bearings. All bearings used in the stand are unsealed to avoid

Table 1 Summary of performance specifications for the ROAMX Hover Test Stand.

Feature	Specification / Description
Hover Test Condition	Rotor plane is greater than two diameters away from the ground.
Motor Cooling	Water-cooled motor allows for continuous testing without risk of overheating (convection cooling of motor is not possible at Mars densities).
Continuous Stall Torque and RPM	83 N·m at 5900 revolutions per minute (RPM).
Sensors	High-accuracy sensors collect performance data (Figure 6). *Thrust:* Three uniaxial Interface SM-100 load cells, ±0.03% full-scale nonlinearity, ±0.01% full-scale nonrepeatability, 440 N full-scale each. *Torque:* Interface TSCF-50, 0.1% full-scale accuracy, 50 N·m full-scale, 50 Nm full-scale.
Safety Factor	$>$ 11 over yield strength under normal operating conditions (higher load capacity possible with future analysis).
Normal Operating Conditions	Thrust: 300 N. Torque: 50 Nm.
Hub Capability	27° collective range. Supports single-rotor testing in two- or four-blade configurations. Single-rotor tests relevant for future Mars helicopters (e.g., hexacopters).
Structural Capacity	Withstands and continues operation after blade out loads of 10 kN.
Balancing	Built-in weight attachment locations on shaft for blade balancing.
Blade Swapping	Hub design facilitates swapping of different blades and blade sets.
Shaft Interface	ROTAX flange shaft allows use of different hubs.
Test Environment	Operates at pressures from 1020 mbar to 5.5 mbar. All components are vacuum-rated and suitable for Earth pressures, enabling testing across a wide Reynolds number range.

Table 2 Experimental Test Conditions for Test Entry 1.

Parameter	ROAMX	Ingenuity
Density [kg/m^3]	0.009, 0.015, 0.023	0.009, 0.015, 0.023
RPM	3300, 3600	3300
Tip Mach Number	0.74, 0.80	0.74

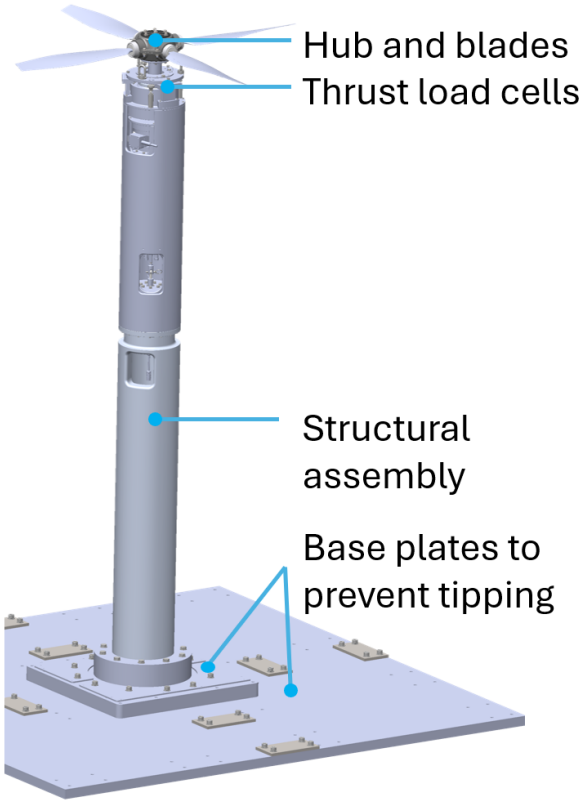

Fig. 2 High-level components of the ROAMX test stand.

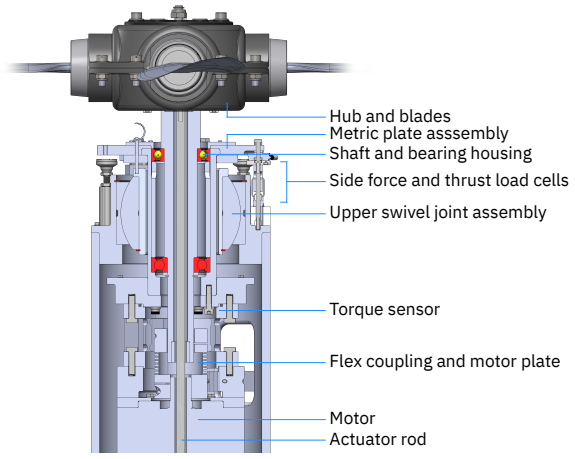

Fig. 3 Components on the metric side of the ROAMX test stand.

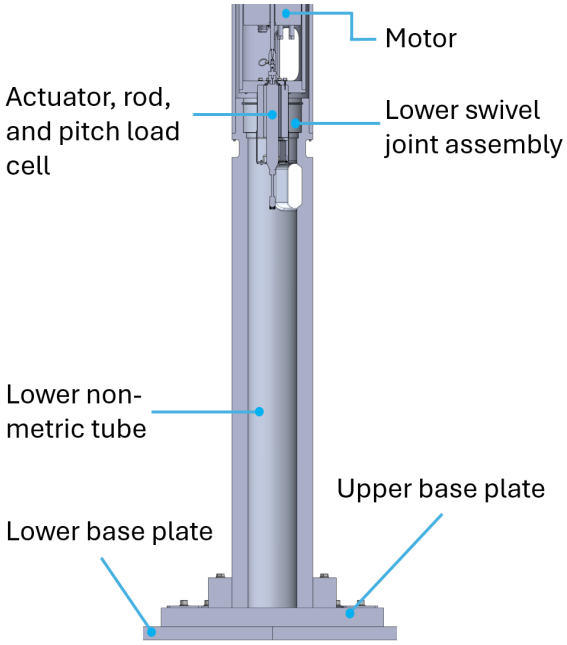

Fig. 4 Components on the non-metric side of the ROAMX test stand.

pressure differentials, and vacuum-compatible grease was selected for critical components to ensure lubricant stability and to prevent volatilization during extended high-RPM operation. Both the motor and the actuator employ vacuum-rated designs from Wittenstein, with material selections and internal tolerances intended to maintain mechanical and thermal performance at low pressure. Similarly, all load cells, diaphragm elements, and temperature sensors were selected to ensure sustained performance under vacuum conditions. These considerations ensured that the RHTS maintained measurement fidelity and mechanical integrity during long-duration rotor testing in near-vacuum conditions representative of the Martian atmosphere.

C. High Tip Mach Number Operation

Due to the low air density on Mars, rotorcraft rely on high rotational speeds to generate sufficient lift. For the ROAMX campaign, the test stand was required to be able to achieve and maintain rotor tip Mach numbers up to approximately $M_{\text{tip}} = 0.95$, corresponding to rotor speeds of $4,300$ RPM for the rotor radius tested in the ROAMX experiment. The motor drive system, bearings, motor cooling approach, and structural elements were therefore required to withstand the associated centrifugal loads, vibratory environment, and torque demands without degradation in performance during extended operation.

D. Load Path and Structural Design Approach

The structural design of the RHTS was driven by the need to support accurate aerodynamic force measurement while withstanding the large inertial loads associated with high tip Mach number rotor operation under Mars aerodynamic conditions. At Mars density, nominal thrust loads are on the order of 100 N, whereas the loss of a blade can impart a lateral blade out load approaching 10 kN. This two-order-of-magnitude difference imposes competing requirements: the measurement system must measure small aerodynamic forces with high fidelity, yet the structural load path must be capable of withstanding extreme blade out loads without risking damage to the PAL facility or the high cost components of the test stand.

Safety factor requirements were established in accordance with the National Full-Scale Aerodynamics Complex (NFAC) Operations Manual Test Planning Guide and the Langley Research Center Wind-Tunnel Model Systems Criteria. For normal operation, primary load-bearing components were required to meet a minimum factor of safety of 3 over yield and 4 over yield strength. Under blade out conditions, rotor testing facilities typically require a minimum factor of safety greater than 1 over ultimate strength. However, as continued long-duration operation was desired for the test stand, all primary components of the RHTS were designed to exceed these requirements, achieving safety factors of at least 2 over yield strength for the blade out load case.

The RHTS incorporates a dedicated safety load path to ensure structural integrity during a blade out event. Under normal operation, axial thrust loads are transmitted through the performance thrust sensors, which form the structural connection between the metric and non-metric sections of the stand. If a blade out event causes the thrust sensors to yield, the load path transfers immediately into the two swivel joints located below the metric section. Each swivel joint contains a sleeve, and upon thrust sensor failure, the bearing housing impacts the swivel joint sleeve, initiating the swivel motion. The upper joint rotates in the direction of the applied lateral load, while the lower joint rotates in the opposite direction, allowing the assembly to accommodate the imposed moment without overstressing the surrounding structure. The heptagonal outer geometry of the swivel-joint housings prevents point loading and distributes reaction forces regardless of the blade-release direction. This configuration ensures that the metric section remains fully constrained and that the motor assembly, located between the two swivel joints, remains protected, thereby preventing damage to the PAL facility and enabling rapid restoration of test capability. A cross-section of the test stand is shown in Figure 5 to illustrate this load path.

To limit damage and minimize test downtime, the thrust sensors were intentionally selected as sacrificial components within the load path. These sensors are low-cost and easily replaceable, and backup sensor assemblies were maintained on site to allow quick return to service of the test stand following a blade out event. The remainder of the stand, including the swivel joints, structural frame, and balance support system, was designed to remain undamaged under blade out loads.

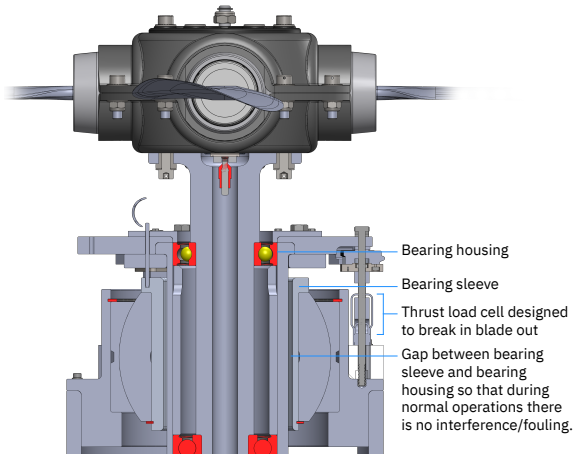

Fig. 5 Depiction of blade out scenario where thrust load cells break.

Geometric constraints were also imposed to limit aerodynamic interference with the rotor inflow. The stand outer diameter was restricted to less than 20% of the rotor diameter, with a maximum allowable stand diameter of 273 mm for a rotor diameter of 1440 mm. This requirement also set limits on the motor outer diameter, which was held to 194 mm to ensure the overall stand footprint remained within the blockage constraint. In addition, the rotor hub is positioned approximately 3 m above the chamber floor to ensure operation outside the ground-effect region (greater than two rotor diameters above the floor).

Collectively, these structural and geometric design decisions establish a load path that provides high measurement fidelity during nominal operation and robust containment capability under blade out conditions, enabling safe and repeatable Mars aerodynamic condition rotor testing.

E. Drive System and Control System Architecture

In Mars rotor testing, the low-density environment presents thermal challenges for electric motors that can limit operation to short duration runs. The ROAMX campaign intended to extend experimental operation to substantially longer duration, enabling the accumulation of sufficient rotor revolutions for high-fidelity averaging and uninterrupted data collection. Achieving this capability under vacuum conditions necessitated a motor and drive system that could operate at high RPM without requiring frequent cool-down intervals. To meet this requirement, the stand employed a custom vacuum-rated Wittenstein

motor with active water cooling, designed to provide the torque and rotational speed required for Mars aerodynamic flight conditions, which enabled extended run times and reduced operational downtime between runs.

The motor is capable of delivering a continuous torque of 83 N·m at 5,900 RPM and a peak torque of 139 N·m. The torque–speed characteristic of the motor enables higher torques and rotational speeds than the required 4,300 RPM, corresponding to a rotor tip Mach number of 0.95. The pitch rod, used for collective actuation, passes through the through-bore along the motor centerline. To satisfy the aerodynamic blockage constraint described in Section II.D, the motor outer diameter was limited to 194 mm, ensuring that the overall stand diameter remained below 20% of the rotor diameter. The motor is water-cooled to support extended operation under vacuum and is remotely controlled from the control room via a Unidrive M700-07400660A4 motor drive.

Collective control is enabled through a four-bladed DUC Hélices variable-pitch propeller (VPP) hub [13]. This hub provides simultaneous pitch adjustment of all blades via a single pitch rod. The hub is employed in aircraft applications such as the Bristell BPM XL8 and engines including the Rotax 912 Edge Performance, demonstrating compatibility with the rotational speeds and blade masses relevant to this test campaign.

A vacuum-rated linear actuator from Wittenstein (Model ALSR038B-030C-171BF-HI1SSN-FBN) provides the required pitch control input for future test entries. The actuator delivers a stroke of 50 mm, can generate a maximum hold force of 1920 N, and has a brake holding force of 1466 N, enabling pitch control across the required collective range under all operating conditions. The actuator interfaces mechanically with the hub pitch rod and is controlled remotely from the control room via a Simco servo drive (Model SIM2007D-CCS-ET00-0000-B00EI). For Test Entry 1, the stand was operated with fixed collective; the actuator and pitch rod were therefore removed, and the collective angle was set manually prior to each chamber pumpdown.

Motor speed is controlled remotely from the PAL control room via motor controller and is capable of closed-loop speed regulation at all desired RPMs. The actuator controller, used in future configurations, allows remote position adjustment with a positioning accuracy of 0.05 mm and a repeat accuracy of 0.01 mm. All control signals, power lines, and feedback channels are routed through vacuum-compatible electrical feedthroughs in the PAL to ensure reliable operation during vacuum testing. Rotor speed measurements are obtained redundantly via the motor's internal encoder and the external optical RPM sensor described in Section II.F.

This drive and control system architecture enables accurate, remotely operated rotor testing under Mars aerodynamic conditions while maintaining the geometric and safety constraints imposed by the structural design.

F. Instrumentation Strategy and Calibration

Accurate thrust and torque measurements are essential to evaluating the aerodynamic performance of rotors. The stand was required to implement thrust and torque sensors which have accuracy of approximately 1% of the expected measurements, which are from around 10-35 N of thrust and 1-10 Nm of torque . These performance requirements placed stringent demands on the load-measurement system: the sensors needed to resolve relatively low aerodynamic forces while simultaneously withstanding the high vibratory and centrifugal loading associated with high-RPM operation in a low-density, low-damping environment. As a result, sensor selection, mounting configuration, alignment tolerances, and the dynamic range of the data acquisition system were all driven by the need to balance measurement sensitivity with structural robustness.

1. Performance Measurement Sensors

Axial thrust was measured using three single-axis Interface SM-100-1357 load cells, with a full-scale reading of 440 N. These sensors provide a nonlinearity of ±0.03% full scale and a nonrepeatability of ±0.01% full scale, supporting the measurement accuracy requirements for thrust coefficient and Figure of Merit calculations. Rotor torque was measured using an in-line Interface TSCF-50NM static reaction torque sensor with 0.1% full-scale accuracy and full-scale reading of 50 Nm. A single-axis pitch force sensor was included in the design to monitor the pitch load transmitted through the actuator assembly and to ensure the maximum allowable pitch load was not exceeded during operation. The sensor was removed for Test Entry 1 since a fixed pitch configuration was used.

2. Safety of Flight Sensors

Rotor imbalance and side force was monitored using three triaxial Michigan Scientific TR3D-B-250 load cells mounted below the performance thrust load cells. These sensors provide real-time measurements of lateral and vertical forces and are used to detect rotor imbalance or anomalous loading conditions during operation. Thermocouples (Evolution P3A-TAPE-REC-PX-1-PFXX) were affixed to the load-cell housings to monitor temperature drift and ensure stable sensor output over long-duration runs.

3. RPM Measurement

Rotor speed was measured both with an external Omron E3S-AR11 optical sensor with retroreflective tape on the rotor hub, and with the motor's internal encoder. The RPM

values from the encoder were used for the data and were cross-checked with the values obtained from the optical sensor.

4. Environmental Instrumentation

Local thermal conditions were monitored using additional thermocouples placed near bearings and performance sensors. Pressure inside the PAL chamber was measured using a Mensor CPC6000 pressure calibrator, with a secondary reference measurement obtained using an MKS 627H absolute pressure transducer. Ambient temperature and humidity were recorded using a Vaisala HMT300 sensor.

5. Sensor Summary

A summary of the full RHTS sensor suite is provided in Table 3 and images of a selection of sensors are shown in Figure 6. All sensors were integrated using vacuum-compatible cabling routed through PAL feedthroughs.

6. End-to-End Calibration Procedure

All performance measurement sensors were calibrated in-place, meaning that the sensors were installed with test hardware in the test configuration and the calibration load was applied as the sensors experienced the loading during testing. The sensors were also calibrated end-to-end instead of in a laboratory setting, meaning they were calibrated with full cable lengths, vacuum feedthroughs, and signal conditioning hardware installed. In addition, check loads were applied before and after each test run to verify measurement repeatability and to identify any thermal or mechanical drift. This procedure ensured that sensor behavior was consistent throughout the test campaign.

7. Torque Sensor Verification

A dedicated torque check was performed using an inline reference rotary torque sensor installed above the motor shaft. The motor provided controlled torque to both the reference sensor and the in-line performance torque sensor. Agreement between the two sensors across the full operating range verified the accuracy of the performance torque measurement. The verification setup and results are shown in Figure 7.

8. Thrust Sensor Verification

Dynamic thrust verification was performed using a two-bladed AWT propeller tested at atmospheric conditions. The thrust–RPM relationship for this rotor had been previously characterized in [14]. Thrust values measured by the RHTS performance thrust sensors matched the reference data, confirming their accuracy. The verification

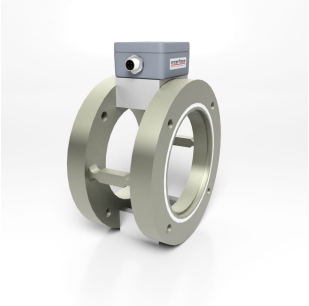

(a) Interface TSCF-50NM torque sensor.

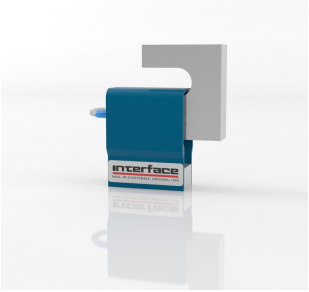

(b) Interface SM-100-1357 thrust sensor.

(c) Omron E3S-A series optical RPM sensor.

Fig. 6 Sensors used in the ROAMX test stand.

configuration and results are presented in Figure 8.

9. Data Acquisition System

The sensor cables were connected to bulkheads on the vacuum and ambient sides of the test facility and were connected to an AstroNova TMX data acquisition system in the control room. The sampling rate for all sensors was set at 5,000 Hz. During testing, data was acquired continuously throughout each run, with each run consisting of an RPM sweep at a set collective angle. Zero points were taken at the beginning and end of each run to account for temperature drift throughout the run.

Table 3 Sensors used in the ROAMX test.

Sensor Use	Sensor Name
Thrust measurement	Interface SM-100-1357 (±0.03% full-scale nonlinearity, ±0.01% full-scale nonrepeatability), 440 N full-scale
Torque measurement	Interface TSCF-50NM (0.1% full-scale accuracy, 50 Nm full-scale)
Side force monitoring measurement	Michigan Scientific TR3D-B-250
Secondary RPM sensor	Omron E3S-AR11
Temperature measurement	Evolution P3A-TAPE-REC-PX-1-PFXX
Pressure measurement	MKS627H
Secondary pressure measurement	Mensor CPC6000 Pressure Calibrator
Environment temperature and humidity sensor	Vaisala HMT300

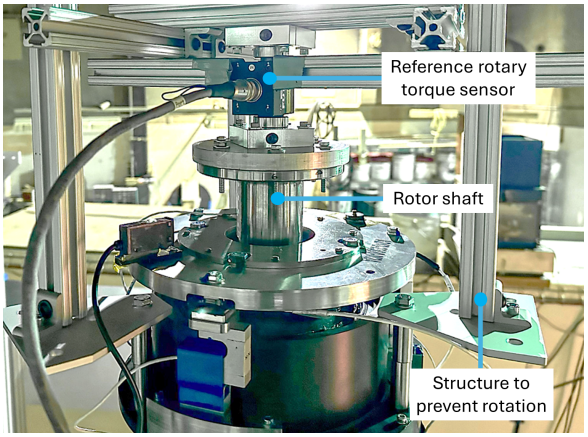

(a) Torque check setup with reference rotary sensor installed above shaft.

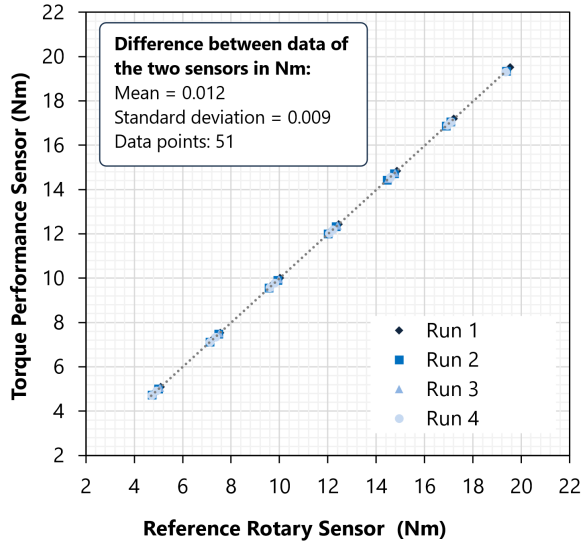

(b) Results from torque check showing agreement between performance torque sensor and reference rotary sensor.

Fig. 7 Torque check setup and results.

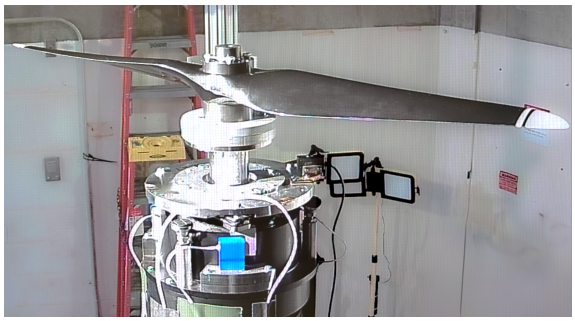

(a) Thrust check setup with AWT propeller installed on shaft of ROAMX stand.

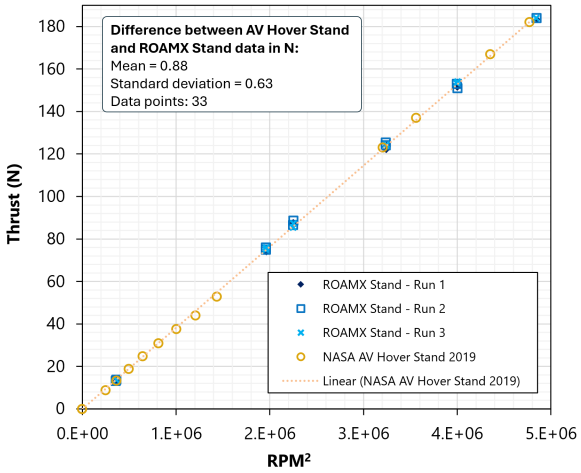

(b) Results from thrust check showing agreement between AWT propeller performance on ROAMX stand and previous test stand.

Fig. 8 Thrust check setup and results.

G. Reusable Test Infrastructure Enabling Rapid and Simplified Rotor Validation

Given the long-term objective of enabling future Mars rotor experimental campaigns, the stand was required to interface seamlessly with PAL infrastructure and support efficient setup and test execution. Critical components including the rotor, hub, and thrust sensors can be replaced with minimal disassembly. The design also emphasized compatibility with existing feedthrough panels and safety protocols, as well as a modular layout that enabled rapid component access, reduced turnaround time, and facilitated reuse in future test campaigns.

In addition, the stringent safety factor requirements maintained for blade out condition enables continued use of the stand with minimal downtime in the unlikely event of blade loss during testing. All hardware except for the load cells can be reused, and the simple blade root interface design allows the blades to be quickly and easily exchanged.

Collectively, these requirements established the operational and design constraints that guided the design and development of the ROAMX experimental test stand. The resulting mechanical design was developed to satisfy these constraints while enabling repeatable, high-fidelity rotor testing under Mars aerodynamic conditions.

III. Test Stand Mechanical Design

The mechanical design of the RHTS was driven by the requirements summarized in Section II and was implemented through a series of custom-machined components. These components establish the primary load paths, support accurate force transmission to the measurement system, and ensure the safety of the RHTS hardware and the PAL facility. Each sub-assembly of custom machined parts is discussed in the following sections.

A. Metric Tube Assembly

The metric tube houses the torque sensor and motor, and is part of the blade out safety system. It is composed of several subassemblies. The metric tube assembly is shown in Fig 9.

1. Lower Heptagon Assembly

The lower heptagon assembly (Fig 10a) fixes the actuator, which is used to pitch the blades, to the rest of the stand. It also includes the bottom heptagon shape that is part of the blade out safety system. To ensure that the heptagon is properly aligned when installed (i.e. that the sides of the heptagon shape are not touching the housing), the shim check system is temporarily used (in blue in the image below). The shims are 2.8 mm thick, which is smaller than the 3 mm gap between the heptagon shape and the housing. This gap indicates that there is no interference between the metric and non-metric assemblies, and is thus critical to prevent fouling of the performance measurements.

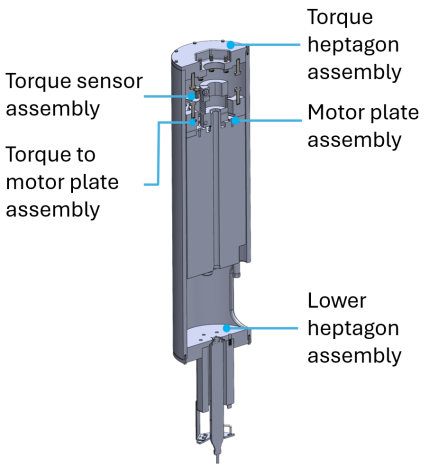

Fig. 9 Metric tube assembly cross-section view.

2. Torque Heptagon Assembly

The torque heptagon assembly (Fig 10b) attaches and fixes the torque sensor to the metric tube via the torque heptagon plate.

3. Torque Sensor Assembly

The torque sensor assembly (Fig 11a) includes the torque sensor and associated bolts. This assembly attaches to the torque heptagon assembly and the torque to motor plate assembly.

4. Motor Plate Assembly

The motor plate assembly (Fig 11b) fixes and attaches the motor to the rest of the metric tube assembly. The motor plate was designed to mate snugly with the motor to ensure alignment. The notches in the motor plate indicate alignment with the motor hoses.

5. Torque to Motor Plate Assembly

The torque to motor plate assembly (Fig 11c) is the connecting piece between the torque sensor and the motor plate. It includes two torque stoppers, which are safety mechanisms to ensure that, if a blade out occurs and parts yield, the motor will not rotate within the assembly. The torque stoppers restrict the rotational movement of the metric tube assembly.

B. Non-Metric Upper Tube Assembly

The non-metric upper tube assembly (Fig 12a) connects to the non-metric side of the thrust load cells. During

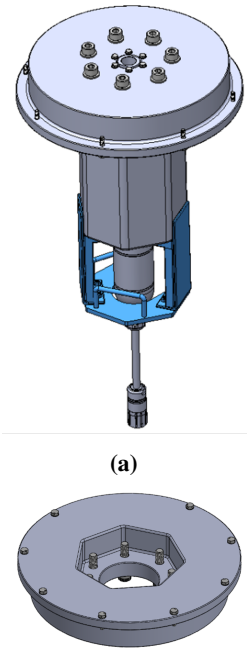

(a)

(b)

Fig. 10 Subfigures show (a) lower heptagon assembly and (b) torque heptagon assembly.

installation of the load cells, the lifting jacks are installed to this assembly. In addition, the upper swivel joint and swivel joint sleeve are part of this assembly. The swivel joint and sleeve are part of the blade out safety system. From the non-metric upper tube assembly, the load cells connect to the metric system. Beneath the non-metric upper tube assembly, the middle non-metric tube is connected.

C. Bearing Housing Assembly

The bearing housing assembly (Fig 12b) connects the rotating and non-rotating systems. It consists of the rotor shaft which interfaces with the off-the-shelf DUC hub, the bearing housing which also serves as the heptagon shape for the blade out safety system, the bearings, and the bearing sleeve. The alignment of all components in this system is critical for the performance of the motor. Tight tolerances were maintained during the manufacturing of the bearing housing and associated components for proper bearing installation. References [15, 16] were consulted to determine appropriate tolerancing requirements. An alignment rod was also designed and manufactured to keep the motor shaft and the shaft in the bearing housing assembly aligned during installation. The rod slides inside both shafts and constrains the alignment to be within 0.0005 inches of misalignment between the motor and bearing assembly. The alignment rod was used during installation to keep the shafts constrained to the aforementioned alignment. The rod could be freely inserted and removed, ensuring the alignment was maintained after assembly. The rod was only temporarily installed for alignment and check fit purposes and is not present in the final testing installation. The method of measurement follows the procedure outlined in [17], of rotating both shafts to override a runout condition. There was found to be less than 0.0005 inches of misalignment between the motor and bearing assembly (indicating an "Alignment Grade 1.2, excellent" alignment condition as seen in Table 4 per [18]).

Table 4 Shaft alignment grades and offsets [18].

Alignment Grade	Alignment Rating	Offset (10^{-3} in)
4.5	Minimal	2.62
2.2	Acceptable	1.28
1.2	Excellent	0.70

D. Metric Plate Assembly

The metric plate assembly (Fig 12c) connects to the metric side of the load cells and also caps the bearings on the bearing housing. During assembly, the entire metric section is lifted into place via eye hooks on the metric plate. The metric plate assembly also includes the side force load cells, which are used for safety of flight monitoring. An infrared RPM sensor is mounted on the metric plate to monitor the RPM of the shaft. The shaft is outfitted with a strip of retro-reflective tape so that the RPM sensor receives a signal every revolution of the shaft, allowing for the calculation of RPM.

E. Swivel Joint Assembly

The swivel joint assembly (Fig 13a) is an assembly of the second swivel joint and bearing sleeve. It sits inside the lower non-metric tube and in case of a blade out, would act along with the lower heptagon (from the lower heptagon assembly) to prevent the blade out load from propagating through the test stand.

F. Lower Non-Metric Assembly

The lower non-metric assembly (Fig 13b) provides the height of the rotor stand such that the rotors are spinning at least two rotor diameters above the ground, to be out of ground effect. It also includes the welded cylinder that allows the entire stand to be bolted to the base plates. The base plates are designed such that the inertial load of the blades will not tip the stand.

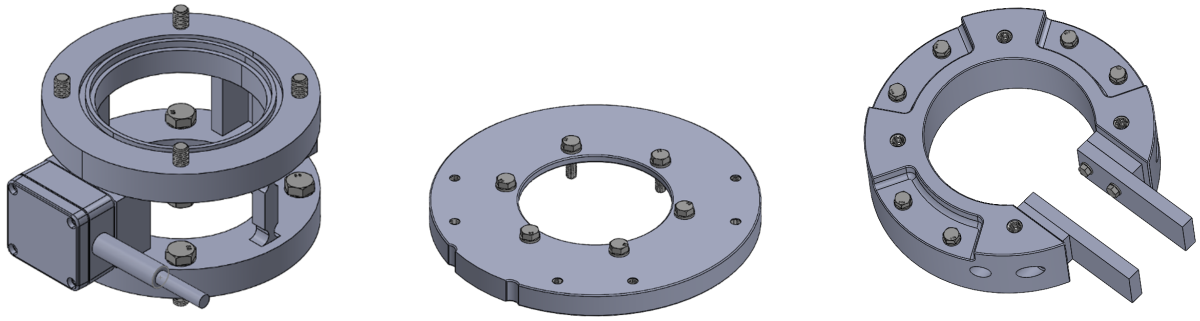

(a) (b) (c)

Fig. 11 Subfigures show (a) torque sensor assembly, (b) motor plate assembly, and (c) torque to motor plate assembly.

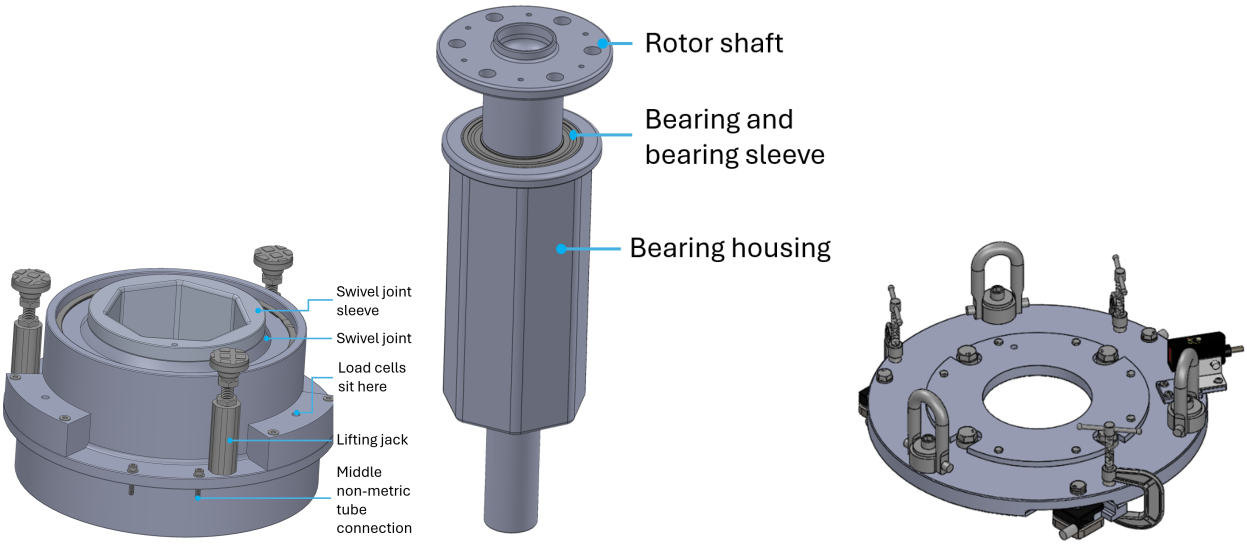

(a) (b) (c)

Fig. 12 Subfigures show (a) non-metric upper tube assembly, (b) bearing housing assembly, and (c) metric plate assembly.

G. Actuator Rod Assembly

The actuator rod assembly (Fig 13c) connects the actuator to the pitching mechanism on the hub. It includes the pitch load cell and actuator rod, and extends all the way through the motor; the assembly is over 40 inches (over 1000 mm) long. The straightness of the rod is critical so that the assembly does not touch the motor, and so that the clevises and threads on either side of the assembly can mate easily. This assembly was removed for Test Entry 1 since the entry was tested in fixed pitch.

IV. Test Stand Loads and Stress Analysis

This section provides an overview of the loads and stress calculations performed for the ROAMX Hover Test Stand. The hand calculated stress analysis for the shaft, tipping analysis, and buckling analysis are shown. A representative case is shown to demonstrate how Finite Element Analysis calculations were performed. In addition, the methodology and formulas used to calculate the applied tightening torque on the fasteners, the stress on the fasteners, and the thread pullout load on the fasteners is shown. To determine loads and constraints for each custom machined part, each part was individually considered under normal operation and blade out condition. Blade out is a condition when any part of the blade comes detached from the stand. This is considered a test specimen failure, and results in large imbalanced loads until the rotor can be brought down to zero RPM. This is usually considered worst case scenario in terms of loading condition for a rotor test stand.

The loads applied for normal operating and blade out conditions are shown in Table 5.

Table 5 Summary of applied loads under normal and blade-out conditions.

Load	Normal	Blade-Out
Thrust (N)	300	300
Side force at rotor plane (N)	100	10 000
Torque (N m)	45	45
Actuator torque (N m)	2	2
Metric section weight (N)	1006	1006
Pitch load (N)	1100	1100

A. Shaft Analysis

The shaft analysis was performed through hand calculations using shear and moment diagram methods and stress concentration factors. As with all of the components, the shaft was analyzed for normal operating conditions as well as blade out loads. There are several loads that are applied to the shaft, including the thrust load, the load of the weight of all of the metric system (including the motor and torque sensor), the pitch load from the blade pitch force, and the reaction forces at the bearing interface locations. The reaction forces at the bearing interface locations are caused by the centrifugal force in blade out and the imbalance in normal operating conditions. Several stress concentration factors were applied and were taken from the Machinery's Handbook [15]. The summary of the shaft material and safety factors is shown in Table 6.

Table 6 Shaft material strength and safety factors.

Quantity	Yield	Ultimate
Material strength (ksi)	145	160
Material strength (MPa)	1000	1103
Safety factor (normal ops)	101.98	112.52
Safety factor (blade out)	3.29	3.63

To calculate the shaft stresses for both normal and blade out operations, the Von Mises stress must be calculated. The first step is to calculate the reactions at the upper and lower bearings. To calculate the reactions, the sum of moments and sum of forces, as well as the distance between rotor plane and the bearing locations, are used, where $d_{r,l}$ is the distance from the rotor plane to the lower bearing, $d_{u,l}$ is the distance between upper bearing to lower bearing, $d_{r,u}$ is the distance between the rotor plane and the upper bearing, CF is the centrifugal force or side force imbalance, F_u is the reaction force on the upper bearing, and F_l is the reaction force on the lower bearing.

CF for blade out is calculated at a tip Mach number of 0.95, or an RPM of 4300. The blade mass m is 0.18 kg and the center of gravity is at $r = 0.28$ m. At r, the Mach number is 0.37, resulting in $v = 126.3$ m/s.

$$CF = \frac{mv^2}{r} \tag{1}$$

This results in $CF = 10$ kN under blade out conditions.

$$\sum M = CF\, d_{r,l} - F_u\, d_{u,l} = 0, \tag{2a}$$

$$F_u = \frac{CF\, d_{r,l}}{d_{u,l}}. \tag{2b}$$

Where Equation 2a is the sum of the moments about the lower bearing and is used to find F_u via Equation 2b. F_l can then be calculated by taking the sum of the forces, where Equation 3b is derived from Equation 3a.

$$\sum F = CF - F_u + F_l = 0, \tag{3a}$$

$$F_l = F_u - CF. \tag{3b}$$

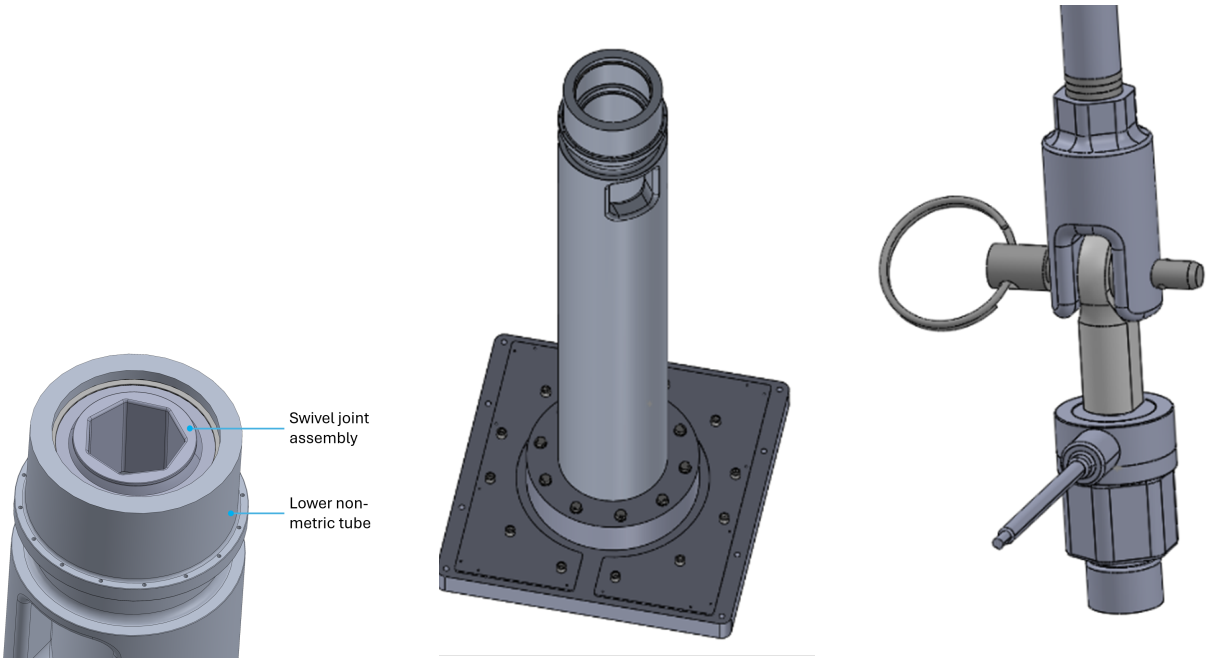

Fig. 13 Subfigures show (a) swivel joint assembly, (b) lower non-metric assembly, and (c) actuator rod assembly.

As seen in Figure 14, the maximum moment occurs at the upper bearing and, given a known CF, can be calculated as:

$$M_{max} = CF \cdot d_{r,u} \tag{4}$$

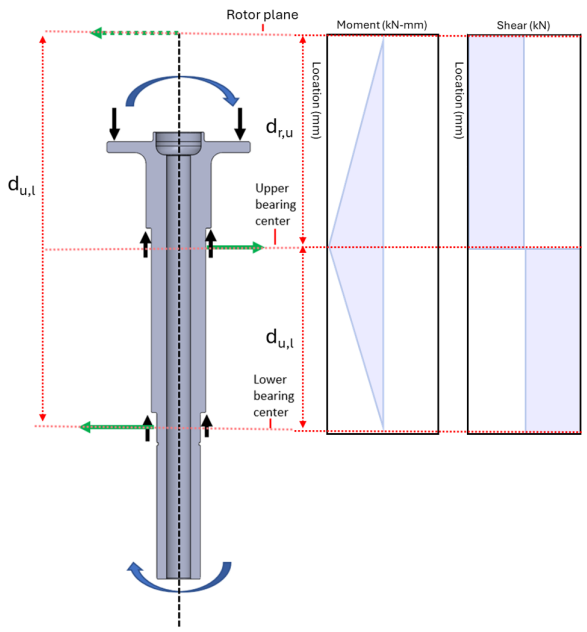

Fig. 14 Shaft moment and shear diagram.

From the maximum moment, the bending stress (σ_b) can be calculated, given the outer shaft diameter d_{shaft} and the moment of inertia I_{shaft}:

$$\sigma_b = \frac{M_{max} d_{shaft}}{2I_{shaft}} \tag{5}$$

The axial stress σ_a is calculated using the axial force F_a (in this case the sum of the weight of the system and the pitch load) and the area of the shaft A_{shaft}:

$$\sigma_a = \frac{F_a}{A_{shaft}} \tag{6}$$

The shear stress from side forces τ_{sf} can be calculated as:

$$\tau_{sf} = \frac{4F_u}{3A_{shaft}} \tag{7}$$

The shear stress from the torque τ_t can be calculated with T as torque and J as the polar moment of inertia as:

$$\tau_t = \frac{T\left(\frac{d_{\text{shaft}}}{2}\right)}{J} \tag{8}$$

Finally, the Von Mises stress on the shaft is calculated. The bending and axial stress, and the side force and torque shear stress are each multiplied by a stress concentration factor shown in Table 7 before they are used in the Von Mises calculation [15].

Table 7 Summary of stress concentration factors.

Notation	Stress Concentration Factor
σ_b	2.48
σ_a	3.00
τ_{sf}	2.48
τ_t	2.10

$$\sigma_{vm} = \sqrt{(\sigma_b + \sigma_a)^2 + 3\left(\tau_{sf} + \tau_t\right)^2} \tag{9}$$

For the shaft under blade out condition, the maximum reaction force was found to be at the upper bearing, where $F_u = 18.3$ kN and the bending moment at the upper bearing was found to be 1.4 kN-m. With the stress concentration factors applied, the Von Mises stress was found to be 304 MPa, resulting in a safety factor of 3.3 over yield for 17-4 PH condition A stainless steel.

B. Base Plate Analysis

The floor of the PAL is concrete; because of the nature of the facility, it cannot be drilled into. Therefore, heavy, wide base plates are needed to prevent tipping under blade out conditions. Powder coated carbon steel is used as the material for the base plates. There is an upper base plate that attaches to the lower non-metric section of the test stand, and there are 4 lower base plates that attach to the upper base plate. The design requirement is that the base plate does not move during blade out. The friction coefficient between concrete and steel was taken from [15], and the calculation in Equation 10 shows that the friction force is higher than the blade out force, which was calculated in Equation 1; therefore, the stand will not slide and the base plate will not move during blade out. Table 8 shows the stress calculations for the base plates and shows that the safety factors are sufficiently high.

$$\sum F = 0 \Rightarrow CF - F_{\text{friction}} = 0, \tag{10a}$$

$$CF = F_f, \tag{10b}$$

$$F_f = \mu N = \mu m g, \tag{10c}$$

$$\mu = 0.55 \text{ (concrete on steel)}, \qquad m = 2500 \text{ kg}, \tag{10d}$$

$$F_f = 0.55 \times 2500 \text{ kg} \times 9.81 \text{ m s}^{-2} = 1.35 \times 10^4 \text{ N}, \tag{10e}$$

$$CF = 1.00 \times 10^4 \text{ N} < F_f \quad \text{(no sliding)}. \tag{10f}$$

Table 8 Structural properties and safety factors for upper and lower base plates.

Property	Upper	Lower
Weight (N)	2648.7	5670.18
Area (mm^2)	122625	538001
Stress (MPa)	0.0216	0.01054
Yield strength (MPa)	248	248
Safety factor	11481	23531

C. Buckling Analysis

A buckling analysis was conducted for several of the components including the actuator rod, the non-metric lower tube and middle tube, the shaft, the bearing housing, and the metric tube. Formulas for the buckling analysis were taken from the Machinery's Handbook and the Professional Engineer Mechanical Handbook [15, 19]. The first step in a buckling analysis is to determine if the column is "long" or "intermediate", and the second step is to calculate the critical buckling load. The slenderness ratio of a column is defined as:

$$S_r = \frac{l}{r_g} \tag{11a}$$

where l is the column length and r_g is the radius of gyration.

$$r_g = \sqrt{\frac{I}{A}} \tag{11b}$$

where I is the area moment of inertia and A is the cross-sectional area.

With the slenderness ratio known, it is possible to determine if the column is "long" or "intermediate" by comparing the slenderness ratio to the column stress determination factor. A column is considered an "intermediate column" if:

$$(S_r)_D = \sqrt{\frac{2\pi^2 E}{K^2 S_y}} \tag{12b}$$

$$S_r \leq (S_r)_D \tag{12a}$$

where S_r is the slenderness ratio.

where $(S_r)_D$ is the column stress determination factor, E is Young's modulus, S_y is yield strength, and K is the effective-length factor.

K, which is the effective length factor, is provided via lookup table based on the boundary conditions of the column [15, 19]. For an intermediate column, the critical buckling load can be calculated as:

$$P_{cr} = A\left[S_y - \frac{K^2}{E}\left(\frac{S_y S_r}{2\pi}\right)^2\right] \tag{13}$$

where P_{cr} is the critical buckling load, A is the cross-sectional area, S_y is yield strength, E is Young's modulus, and S_r is the slenderness ratio.

If the slenderness ratio is greater than the column stress determination factor, the column is considered a "long" column and the critical buckling stress can be calculated as:

$$P_{cr} = \frac{\pi^2 E I}{(Kl)^2} \tag{14a}$$

where P_{cr} is the *critical axial load*, E is Young's modulus, I is the moment of inertia, K is the effective-length factor, and l is the unbraced column length.

$$\sigma_{cr} = \frac{P_{cr}}{A} = \frac{\pi^2 E}{\left(\frac{Kl}{r_g}\right)^2} \tag{14b}$$

where σ_{cr} is the *critical buckling stress*, A is the cross-sectional area, $r_g = \sqrt{\frac{I}{A}}$ is the radius of gyration, and $\frac{Kl}{r_g}$ is the effective slenderness ratio.

D. Finite Element Analysis

Finite Element Analysis (FEA) was conducted for each custom machined part within each assembly. The forces and moments were determined for each part individually, and close attention was paid to where the loads were applied and where the fixtures were applied. This was done for two conditions: normal operating conditions and blade out condition. Mesh refinement studies were conducted for each case to ensure that stress convergence was reached. SolidWorks was used to conduct the FEA stress calculations. The safety factors were calculated based on the maximum Von Mises stress calculated. Maximum deflection was also collected for each case. An example FEA and deflection calculation for normal loads is shown in Fig 15 for the bearing housing, and the parameters for the study are shown in Table 9.

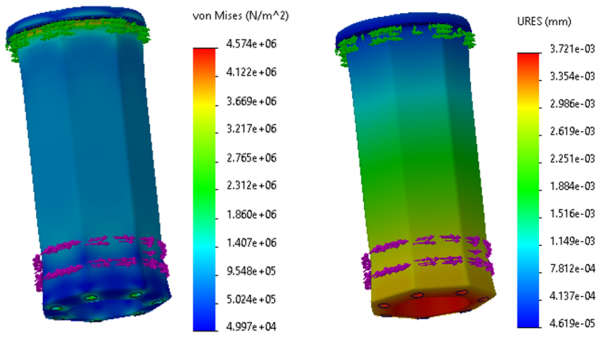

(a) Von Mises stress distribution (SolidWorks FEA). **(b) Total deflection contours (SolidWorks FEA).**

Fig. 15 SolidWorks FEA results for the bearing housing showing stress and deflection.

Table 9 Bearing housing: setup, loads, and FEA results.

Part	Bearing housing
Placement in assembly	Bearings mounted inside housing; shaft passes through housing.
Material	7075-T6 aluminum, yield strength 505 MPa.
Fixtures	Fixed underneath top lip.
Applied loads	• Torque: 50 N m on flat faces. • Side force at rotor plane: 100 N; bearing reactions 190 N and 90 N (opposing). • Pitch tension: 1100 N at top of flange. • Weight: 981 N at top of flange.
Von Mises stress	4.6 MPa (max).
Safety factor (yield)	SF = $\sigma_y/\sigma_{\max}$ = 505/4.6 = 110.
Max deflection	0.004 mm.

E. Fastener Analysis

Each bolt and fastener was analyzed to ensure that the clamping load realized by the fasteners is higher than the applied load. The torque specification to be applied on each fastener is also calculated. When calculating the stress on each bolt, the NASA wind tunnel model criteria specifies that the loads should be applied to the fastener itself (not assuming that the clamping load is taking the forces) to ensure that the fastener would not break even if the clamping load was lost. Thread pull out is also a required calculation, as well as the helicoil pull out where necessary. For each fastener, the torque specification is calculated based on the required pre-load on the fastener given the forces that the fastener experiences during normal and blade out operations. Where a given fastener experiences a shear load, shoulder bolts are used so that the shoulder takes the load instead of the threaded portion of the fastener taking the load. Shigley's Mechanical Engineering Design was referenced for the fastener pitch; tensile stress area; minor diameter; minimum proof, tensile, and yield strengths; and torque factors [20]. The NASA Fastener Design Manual was referenced for the formula for pullout load for threaded holes [21].

1. Pre-Load on Fasteners

To calculate the pre-load on the fasteners, the nominal (d_n), minor (d_r), pitch (d_p) and mean diameters (d_m), as well as the pitch (f_p) (for metric fasteners) and threads per inch (TPI) (for inch fasteners) of the fasteners are needed. The minor area (A_m) and tensile stress area (A_t)

are calculated from those diameters. A_m is calculated directly from the minor diameter. A_t for threaded fasteners is defined using a standard empirical relationship that accounts for the reduced cross section at the thread root. The minimum proof strength, given the property class of the fastener, is also needed.

Diameter calculations for metric fasteners:

$$d_r = d_n - 1.226\,869\,f_p \tag{15a}$$
$$d_p = d_n - 0.649\,519\,f_p \tag{15b}$$
$$d_m = \frac{d_r + d_p}{2} \tag{15c}$$

Diameter calculations for inch fasteners:

$$d_r = d_n - \frac{1.299\,038}{\text{TPI}} \tag{16a}$$
$$d_p = d_n - \frac{0.649\,519\,05}{\text{TPI}} \tag{16b}$$
$$d_m = \frac{d_r + d_p}{2} \tag{16c}$$

$$A_m = \frac{\pi d_r^2}{4} \tag{16a}$$

For metric fasteners,

$$A_t = \frac{\pi}{4}\left(d_n - 0.9382 f_p\right)^2 \tag{16b}$$

and for inch fasteners,

$$A_t = \frac{\pi}{4}\left(d_n - \frac{0.9743}{\text{TPI}}\right)^2 \tag{16c}$$

The proof load (PL) is calculated by:

$$\text{Proof Load} = (\text{Minimum Proof Strength})\, A_t \tag{17}$$

The pre-load force ($F_{b,p}$) is the force that is applied to the fastener when applying torque, and is a fraction of the proof load. To be able to re-use fasteners, $F_{b,p} \leq Proof\ Load$, and Shigley recommends including a pre-load factor of 0.75 [20]:

$$F_{b,p} = (\text{Proof Load})(\text{Pre-Load Factor}) \tag{18}$$

However, the amount of $F_{b,p}$ should be chosen by the designer depending on the application. For example, if $F_{b,p}$ is too high, thread pull out can become an issue. Thus, for this application, the pre-load factor was kept at 0.75 or below to ensure thread pullout was not an issue.

To calculate the torque specification (T) that is specified during assembly, a torque coefficient (k) is needed that describes the conditions, such as lubrication and surface finish, on the fastener as it is tightened.

$$T = k F_{b,p} d_n \tag{19}$$

The friction due to the pre-load (Fr_p) can be calculated as the friction coefficient (μ) multiplied by the number of fasteners sharing the preload (N) and the pre-load force ($F_{b,p}$)

$$Fr_p = \mu N F_{b,p} \tag{20}$$

If Fr_p is greater than the side force applied, the side force will be taken by the pre-load instead of the fastener.

2. Stress on Fasteners

To calculate the stress on the fastener, first the pre-load force ($F_{b,p}$), normal force ($F_{b,n}$), shear force ($F_{b,s}$), and bending moment (M_b) are calculated. Then, the respective stresses (σ_p, σ_n, τ_s, σ_b) can be calculated:

$$\sigma_p = \frac{F_{b,p}}{A_t} \tag{21a}$$
$$\sigma_n = \frac{F_{b,n}}{A_t} \tag{21b}$$
$$\tau_s = \frac{F_{b,s}}{A_s} \tag{21c}$$
$$\sigma_b = \frac{32 M_b}{\pi d^3} \tag{21d}$$

$A_s = A_t$ when the shear force is applied on the shank of the fastener instead of on the threads. If the shear force is applied on the threads, A_s is calculated using the minor diameter of the fastener.

Von Mises stress, σ_{VM} can then be calculated as:

$$\sigma_{\text{VM}} = \sqrt{\left[\sigma_p + (\sigma_n + \sigma_b)\right]^2 + 3\,(\tau_s)^2} \tag{22}$$

3. Thread Pull Out

Thread pull out occurs when the internal thread that a fastener is threaded into is compromised. The length of engagement (L) needs to be calculated for threaded holes, especially if the material that is being threaded into is weaker than the material of the fastener. To calculate the thread pull out load (P), the material yield stress (σ_y) is needed.

$$P = \frac{\pi d_m \sigma_y L}{3} \tag{23}$$

The NASA Fastener Design Manual Ref [21] recommends using the empirical value of $1/3$ because of the mismatch in threads - if the fastener threads and the tapped hole threads fit perfectly together, the factor would instead be $1/2$.

V. Analysis Results

The tables below show the summary from the analysis that was conducted for the ROAMX test stand.

A. FEA

Table 12 is a summary of the results for the FEA cases. All safety factors over yield strength are well above 4 under nominal loading conditions, and above 2 for blade out condition. Although typical facility requirements require a safety factor of 1 over yield strength for blade out condition, the goal for this test stand was to have at least a safety factor greater than 2 over yield. Because the blades that are being tested on the stand are experimental blades, the likelihood of blade out is greater than for blades that have been extensively tested. Thus, it was desired to ensure that the test stand could easily withstand blade out and that testing could continue. During Test Entry 1 of the testing, no blades broke during testing, so the stand was not tested under the harsh blade out condition.

B. Buckling Analysis

The results from the buckling calculations under operational loads are shown in Table 10. None of the components experience loads that are close to the critical buckling loads, and the minimum safety factor of 6 is for the actuator rod.

Table 10 Buckling analysis summary.

Component	Safety Factor
Actuator Rod	6
Non-Metric Lower Tube	882
Non-Metric Middle Tube	1173
Shaft	439
Bearing Housing	372
Metric Tube	999

C. Sensors

The sensors were sized to be able to accurately read the loads that will be applied to them. Thus, the safety factor for the sensors is not expected to be high. From the NASA wind tunnel model criteria, a monitored load is required to have a safety factor of 2. Thus, the thrust load cells have a safety factor of 2 and were chosen specifically to have that safety factor. Safety factors for the sensors are shown in Table 11.

D. Fasteners

The results for the fastener analysis are shown in Table 13. The minimum safety factor requirements are 4 under normal operating conditions and 1 under blade out. However, for this test stand, it was desired to have all safety factors greater than 2 under blade out conditions; this criteria is successfully met as seen in Table 13.

VI. Test Stand Performance

The first use of the RHTS occurred during Test Entry 1, in which full-scale ROAMX rotor blades and full-scale Ingenuity aerodynamic replica blades were operated under Mars aerodynamic conditions. The purpose of this section is to document the performance of the test stand itself during the test entry. Aerodynamic and performance results for the ROAMX rotor are reported separately and are not repeated here [11, 22].

A. Drive System Performance During Test Entry 1

Throughout Test Entry 1, the vacuum-rated motor demonstrated stable operation across the commanded speed range, achieving rotational speeds up to 4,000 RPM with ease and maintaining steady RPM within 5 RPM of the set point. Motor torque remained consistent with the specified torque–speed characteristic, and no abnormal heating was observed under reduced pressure operation. These results confirm that the drive system performed as required to support Mars rotor testing. The stand is capable of operation at higher RPM and torque, which was out of the scope for Test Entry 1. Higher RPM will be investigated in future test entries.

B. Measurement System Performance During Test Entry 1

All performance-measurement sensors operated as intended during Test Entry 1. Thrust and torque sensors exhibited stable, low drift behavior, and their calibrated responses remained consistent with the end-to-end calibration described in Section II. The redundant RPM measurements obtained from the optical sensor and the motor encoder remained in close agreement across all operating conditions. Side force sensors responded predictably, confirming correct operation of the imbalance monitoring system. Sensor performance therefore met the accuracy and stability requirements defined in Section II.

C. Structural Safety System Behavior

Although Test Entry 1 did not involve blade out–level loads since no blade out occurred, the structural safety system was verified to behave mechanically as designed. The swivel-joint assembly and surrounding structural hardware were inspected during operation and after each test, with no evidence of misalignment, binding, or unintended load transfer. These observations confirm correct installation and nominal mechanical behavior of the safety system.

D. Operational Readiness Demonstrated by Test Entry 1

The stand's performance during Test Entry 1 demonstrated that the RHTS meets all functional, mechanical, and measurement requirements necessary for Mars rotor testing.

Table 11 Summary of sensor load ratings and safety factors.

Name	Rated Load (Total)	Highest Expected Load – Normal Ops	Rated Overload	Maximum Rated Load	Safety Factor
Thrust Load Cell	1335 N	1005 N	2000 N	—	2
Torque Sensor	50 N m	45 N m	75 N m	200 N m	4

The stand operated reliably under low pressure conditions, demonstrated by the stand's ability to reach 4000 RPM without exceeding operational limits on temperature or measurements; the stand maintained measurement fidelity across the required operating envelope at each test density, with check loads proving repeatable before and after each run; and the stand exhibited safe structural behavior, as it did not experience any hardware failure during performance testing. These results establish that the RHTS is ready to support future ROAMX test entries and broader Mars rotorcraft development efforts.

VII. Conclusions

The ROAMX Hover Test Stand (RHTS) was developed to provide a high-fidelity experimental platform for evaluating rotor performance under Mars aerodynamic conditions. The design meets the aerodynamic, structural, measurement, and operational requirements necessary to support current and future Mars rotorcraft development efforts.

The stand incorporates several key capabilities, including accurate thrust, torque, and RPM measurement; a vacuum-compatible drive and measurement system; a structural safety architecture that satisfies NASA requirements; and a low-blockage mechanical configuration that minimizes aerodynamic interference. The modular interface provided by the DUC variable pitch hub enables rapid integration of new experimental blade sets and supports future implementation of remote collective control.

Test Entry 1 demonstrated that the stand operates as intended under both ambient and Mars conditions. The drive system achieved the required rotational speeds, up to 4000 RPM, while demonstrating stable thermal behavior, and all performance sensors exhibited the accuracy necessary for high-fidelity rotor performance characterization. The structural safety system showed correct mechanical behavior under nominal loading. Detailed aerodynamic results for the ROAMX rotor tested during Test Entry 1 are reported separately in [11].

The successful demonstration of these capabilities establishes the RHTS as a long-term reusable asset. The stand significantly enhances NASA's ability to conduct Mars rotor experiments with higher fidelity, expanded operating envelopes, and reduced turnaround time compared to previous test platforms.

Future work includes activation of the remote collective control capability, integration of additional instrumentation as required for upcoming campaigns, and application of the stand to new rotor designs generated through ongoing ROAMX and Mars rotorcraft research. These efforts will build upon the validated foundation established by the RHTS and enable continued advancement of Mars rotor aerodynamics and vehicle development.

Future research supporting Mars helicopter development that this test stand can support includes:

- testing of high solidity rotors for high lift Mars rotorcraft;
- testing of rotors designed with 3-dimensional coupled structural and aerodynamic analysis;
- testing of rotors with visualization techniques implemented in the experimental facility;
- various rotor tests at Earth atmosphere, Mars atmosphere, or at any density in between, to characterize rotor performance at a wide range of Reynolds numbers.

The ROAMX Hover Test Stand establishes a robust experimental capability for Mars aerodynamic condition rotor testing within the Planetary Aeolian Laboratory. By enabling high-fidelity, repeatable evaluation of advanced rotor designs, the stand supports continued progress toward more capable and scientifically productive Mars rotorcraft missions.

Acknowledgments

The ROAMX project is funded through the Early Career Initiative program in NASA's Science Technology Mission Directorate (STMD).

The authors would like to thank the NASA Ames machine shop, especially Rob Kornienko, Vince Derilo, and Ron Hovland, and Marissa Melo. The authors would like to thank Niklas Beck and Michael Derderian for many hours of consultation regarding their hardware. Larry Young is thanked for his constant encouragement. Dr. William Warmbrodt is thanked for his excellent leadership. Carl Russell and Gina Willink are thanked for their support. Charles Cornelison, Antonio Cervantes, Alfredo Perez, Steve Naldoza, Ken Smith, and JP Wiens are thanked for their support regarding PAL operations. Sarah Conley and Michelle Dominguez are thanked for their insights.

Table 12 Safety factors over yield strength for major components under normal operations and blade out conditions.

Name	Material	SF Over Yield (Normal Ops)	SF Over Yield (Blade Out)
Shaft	440C stainless steel	102	3.2
Bearing sleeve	6061 aluminum T6	97	97
Shaft bearing clip ring washer	17-4 stainless steel	11	11
Bearing housing	7075 aluminum T6	112	2.4
Metric plate	17-4 stainless steel	24	2.4
Metric plate cap	17-4 stainless steel	60	2.1
Heptagon plate	7075 aluminum T6	39	2.2
Metric tube	6061 aluminum T6	50	3.1
Actuator heptagon plate	7075 aluminum T6	15	2.5
Torque stopper rectangle	7075 aluminum T6	*	7
Motor to torque sensor interface	6061 aluminum T6	240	240
Motor plate	6061 aluminum T6	33	33
Rod to ball joint	7075 aluminum T6	28	28
Actuator rod	7075 aluminum T6	6	6
Actuator rod to pitch load cell interface	7075 aluminum T6	17	17
Load cell connector plate	17-4 stainless steel	38	**
Stand to load cell plate	7075 aluminum T6	37	**
Upper non-metric tube	6061 aluminum T6	209	8.6
Middle non-metric tube	6061 aluminum T6	68	3.4
Lower non-metric tube	6061 aluminum T6	126	2.3
Base plate upper	A36 steel	11481	5.3
Base plate lower	A36 steel	23531	17
Large spacer	A52100 steel	327.5	**
Thin spacer	1008–1010 carbon steel	102.5	**

*Not engaged during normal operations (no load transfer).
**Not engaged during blade out (no load transfer).

Table 13 Fastener Safety Factors (SF) Summary

Fastener Size	**Name**	Von Mises Stress Normal Ops	Von Mises Stress Blade Out	Fastener Pull Out	Clamping Load Normal Ops	Clamping Load Blade Out
M6	Blade bolt**	–	2.6	–	–	–
M16	Top base plate to lower base plate**	–	24.3	5.5	–	2.2
M5	Torque stopper*	5.9	–	6.9	4.5	–
M6	Actuator rod*	17.2	–	2.8	3.5	–
M6	Load cell interface*	6.9	–	6.9	2.1	–
M6	Load cell*	6.9	–	6.9	2.1	–
M16	Actuator*	18.4	–	6.5	2.4	–
M3	Shim*	10.3	–	6.6	6.2	–
M3	Shim holder*	20.5	–	8.9	12.3	–
M3	Actuator*	16.1	–	2.0	8.1	–
M8	Actuator plate**	–	14.1	5.9	–	9.4
M6	Motor plate*	49.9	–	2.7	37.7	–
M6	Motor to torque interface*	69.3	–	10.6	37.5	–
M4	Lower metric tube**	–	4.1	9.7	–	3.8
M10	Torque sensor*	89.1	–	5.9	86.7	–
M8	Bearing housing**	–	6.7	5.9	–	4.4
M4	Upper metric tube**	–	2.1	6.0	–	2.2
M4	Middle to lower non metric tube**	–	2.0	7.9	–	12.1
M4	Upper to middle non metric tube**	–	3.5	10.3	–	24.1
1/4-20	Dummy load cell blocks*	18.8	–	7.7	6.2	–
M3	Bearing cap*	17.3	–	4.4	12.9	–
M8	Metric plate*	–	3.1	3.4	–	2.3
M16	Lower non-metric tube to base**	–	4.1	2.13	–	2.0

* Fastener not subjected to blade out loads.
** Analysis for normal operations not shown since blade out safety factor > 2.

References

[1] NASA, "NASA's Ingenuity Mars Helicopter Succeeds in Historic First Flight," NASA News Release, Apr. 2021. URL https://www.nasa.gov/news-release/nasas-ingenuity-mars-helicopter-succeeds-in-historic-first-flight/, accessed: 2025-08-11.

[2] NASA, "ROAMX Testing in the Planetary Aeolian Laboratory (PAL) at NASA Ames Research Center," https://www.nasa.gov/general/roamx-testing-in-the-planetary-aeolian-laboratory-pal-at-nasa-ames-research-center/, March 2025. Accessed: 2025-08-09.

[3] Cummings, H. V., Perez Perez, B. N., Koning, W. J. F., Johnson, W. R., Young, L. A., Haddad, F. B., Romander, E. A., Balaram, J. B., Tzanetos, T., Bowman, J., Wagner, L. N., Withrow-Maser, S. N., Isaacs, E., Toney, S., Shirazi, D., Conley, S. A., Pipenberg, B. T., Datta, A., Lumba, R. T., Chi, C., Smith, J. K., Cornelison, C. J., Perez, A., Nonomura, T., and Asai, K., "Overview and Introduction of the Rotor Optimization for the Advancement of Mars eXploration (ROAMX) Project," *VFS Aeromechanics for Advanced Vertical Flight Technical Meeting*, Vertical Flight Society, San Jose, CA, 2022.

[4] Koning, W. J. F., Johnson, W. R., and Grip, H. F., "Improved Mars Helicopter Aerodynamic Rotor Model for Comprehensive Analyses," *44th European Rotorcraft Forum*, Delft, The Netherlands, 2018. URL https://rotorcraft.arc.nasa.gov/Publications/files/Koning_2018_TechMx.pdf.

[5] Koning, W. J. F., Romander, E. A., Perez Perez, B. N., Cummings, H. V., and Buning, P., "On Improved Understanding of Airfoil Performance Evaluation Methods at Low Reynolds Number," *AIAA Journal*, 2023. https://doi.org/10.2514/1.C037023, URL https://rotorcraft.arc.nasa.gov/Publications/files/1.c037023.pdf.

[6] Koning, W. J. F., Perez Perez, B. N., Cummings, H. V., Romander, E. A., and Johnson, W. R., "Overview of Rotor Hover Performance Capabilities at Low Reynolds Number for Mars Exploration," *50th European Rotorcraft Forum*, Marseille, France, 2024.

[7] Koning, W. J. F., Perez Perez, B. N., Cummings, H. V., Romander, E. A., and Johnson, W. R., "ELISA: A Tool for Optimization of Rotor Hover Performance at Low Reynolds Number in the Mars Atmosphere," *Vertical Flight Society Sixth Decennial Aeromechanics Specialists' Conference*, Vertical Flight Society, Santa Clara, CA, 2024.

[8] Koning, W. J. F., Perez Perez, B. N., Cummings, H. V., Romander, E. A., and Johnson, W. R., "ELISA: A Tool for Optimization of Rotor Hover Performance at Low Reynolds Number in the Mars Atmosphere," *Journal of the American Helicopter Society*, Vol. 69, No. 4, 2024. https://doi.org/10.4050/JAHS.69.042005.

[9] Koning, W. J. F., Perez Perez, B. N., Cummings, H. V., Nagata, T., Kanzaki, Y., Kasai, M., Miyagi, M., Nonomura, T., Asai, K., Caros Roca, L., Buxton, O., and Vincent, P., "Experimental Results for Mars Rotorcraft Airfoils (roamx-0201 and clf5605) at Low Reynolds Number and Compressible Flow in a Mars Wind Tunnel," NASA Technical Memorandum NASA–TM–20240004230, National Aeronautics and Space Administration, Ames Research Center, Moffett Field, CA, Apr. 2024. URL https://rotorcraft.arc.nasa.gov/Publications/files/NASA-TM-20240004230.pdf.

[10] Caros, L., Koning, W. J. F., Nagata, T., Asai, K., Buxton, O., Perez Perez, B. N., Romander, E. A., Nonomura, T., Cummings, H. V., and Vincent, P., "Computational and Experimental Comparison of CLF5605 and roamx-0201 Martian Helicopter Rotor Airfoils," , 2025. URL https://arxiv.org/abs/2511.14934.

[11] Perez Perez, B. N., Cummings, H. V., Koning, W. J. F., Haddad, F. B., Sheikman, A. L., Cornelison, C. J., Perez, A., Cervantes, A., Wright, S. J., Romander, E. A., Johnson, W. R., Smith, J. K., Lumba, R., Chi, C., Donovan, M., Datta, A., Nagata, T., Asai, K., Nonomura, T., Caros Roca, L., Buxton, O., and Vincent, P., "Guidelines and Designs for Helicopter Airfoils and Blades for Mars Applications with Experimental Validation," *AIAA Scitech 2026 Forum*, Orlando, FL, 2026.

[12] NASA Ames Research Center, Thermophysics Facilities Branch, "Planetary Aeolian Laboratory (PAL)," https://www.nasa.gov/thermophysics-facilities-branch-planetary-aeolian-laboratory/, 2023. Accessed: 2025-08-07.

[13] DUC Hélices, "Certificates and Approvals," https://www.duc-helices.com/en/our-certificates-and-approvals, 2025. Accessed Nov. 20, 2025.

[14] Perez Perez, B. N., "Forward Flight Rotor Performance at Martian Atmospheric Densities and Sensitivity to Low Reynolds Numbers," *Proceedings of the Aeromechanics for Advanced Vertical Flight Technical Meeting*, Vertical Flight Society, San Jose, CA, USA, 2020. URL https://rotorcraft.arc.nasa.gov/Publications/files/Brenda_Natalia_Perez_Perez_TVF_2020.pdf.

[15] Oberg, E., Jones, F. D., Horton, H. L., Ryffel, H. H., and McCauley, C. J., *Machinery's Handbook*, 32nd ed., Industrial Press, New York, NY, 2024.

[16] SKF Group, "Principles of Rolling Bearing Selection," https://www.skf.com/us/products/rolling-bearings/principles-of-rolling-bearing-selection, 2025. Accessed: 2025-08-11.

[17] Piotrowski, J., *Shaft Alignment Handbook*, 3rd ed., CRC Press, Boca Raton, FL, 2006.

[18] American National Standards Institute (ANSI), and Acoustical Society of America (ASA), "Shaft Alignment Methodology, Part 1: General Principles, Methods, Practices, and

Tolerances," ANSI/ASA S2.75 Part 1, 2017. Approved June 6, 2017; Reaffirmed June 19, 2020.

[19] NCEES, *PE Mechanical Engineering: Machine Design and Materials, HVAC and Refrigeration, or Thermal and Fluid Systems Reference Handbook*, National Council of Examiners for Engineering and Surveying, 2024. URL https://help.ncees.org/article/87-ncees-exam-reference-handbooks.

[20] Budynas, R. G., and Nisbett, J. K., *Shigley's Mechanical Engineering Design*, 12th ed., McGraw-Hill Education, New York, 2020.

[21] Barrett, R. T., "Fastener Design Manual," NASA Reference Publication NASARP1228, National Aeronautics and Space Administration, Lewis Research Center, Mar. 1990.

[22] Perez Perez, B. N., Cummings, H. V., and Koning, W. J. F., "Data Report for the Rotor Optimization for the Advancement of Mars eXploration (ROAMX) Hover Test," NASA Technical Memorandum NASA–TM–20250010259, National Aeronautics and Space Administration, Ames Research Center, Moffett Field, CA, Nov. 2025.